DESY 98–052
hep–ph/9805436
May 1998

ISSN 0418–9833

Jet Production in Deep Inelastic Electron-Photon Scattering at e^+e^- Colliders in Next-to-Leading Order QCD

B. Pötter
II. Institut für Theoretische Physik*, Universität Hamburg
Luruper Chaussee 149, D-22761 Hamburg, Germany
e-mail: poetter@mail.desy.de

Abstract

A complete next-to-leading order QCD calculation of deep inelastic electron-photon scattering including direct and resolved real photon components is presented. Soft and collinear singularities are extracted using the phase space slicing method. Application of the results for the prediction of single- and dijet cross sections at the LEP e^+e^- collider are presented, using the Snowmass jet definition. The dependence of the cross sections on the transverse momentum and on the rapidities of the jets are discussed.

*Supported by Bundesministerium für Forschung und Technologie, Bonn, Germany, under Contract 05 7 HH 92P (0), and by EEC Program *Human Capital and Mobility* through Network *Physics at High Energy Colliders* under Contract CHRX–CT93–0357 (DG12 COMA).

1 Introduction

The production of jets with large transverse momenta p_T in $\gamma\gamma$ reactions with both photons being quasi-real has been studied at TRISTAN [1] for quite some time and more recently at LEP [2]. The presence of a large scale in the process allows perturbative QCD calculations. These calculations are available at next-to-leading order (NLO) in QCD [3, 4, 5, 6] and the agreement of the predictions with experimental data is good (see e.g. [7]).

In order to reliably understand the hadronic structure of the photon also the process should be studied where one of the incoming photons has a large virtuality [8, 9, 10]. The scattering of virtual on real photons, which is the analog to deep inelastic electron-proton (ep) scattering, can be achieved in e^+e^--colliders by a single-tag experiment, i.e., one of the leptons is detected under a certain angle and the other escapes unobserved in the beampipe. Single-tag experiments have recently been performed at the LEP storage rings and the results of these measurements are expected in the near future [11]. Some studies of deep inelastic electron photon jet cross sections in leading-order (LO), i.e. $\mathcal{O}(\alpha^2)$, have been done in [12]. A NLO QCD calculation of jet cross sections in $\gamma^*\gamma$ collisions for relatively small virtualities up to 10 GeV^2 has been performed in [13], but without considering the longitudinal photon polarization.

The simplest diagram contributing to the deep inelastic electron photon jet cross section in LO is the quark parton model (QPM) diagram, see Figure 1. The real photon and the virtual photon couple directly to the charge of the bare quark, producing two final state jets. This so-called direct process can be distinguished from resolved processes, where the real photon serves as a source of partons (quarks and gluons) that interact with the virtual photon. In addition to the high p_T jets from the hard scattering, the resolved contribution is accompanied by a "spectator jet" (or photon remnant jet) with small p_T. It has been discussed in [14] that both contributions are of the same order in the strong coupling constant. Note, that the contribution involving the resolved real photon is traditionally called *single-resolved* in $\gamma\gamma$ scattering. We will call this contribution

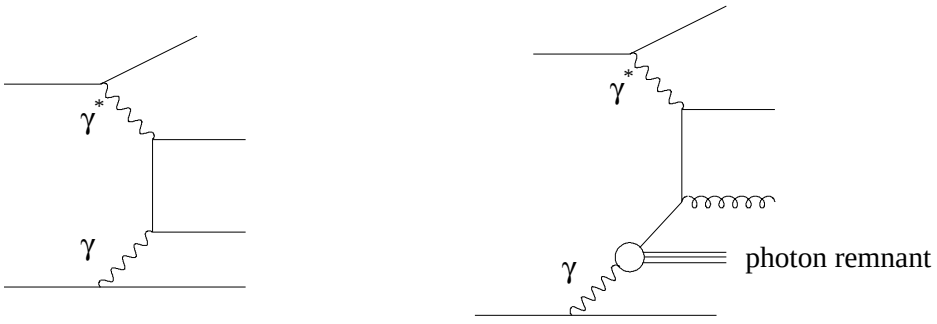

Figure 1: Examples of LO processes in deep inelastic electron photon scattering from e^+e^- collisions. Left: direct contribution (QPM diagram). Right: quark initiated resolved process.

simply *resolved* for ease of writing. Similar to *ep*-scattering, one motivation for studying deep-inelastic $e\gamma$-scattering is to obtain information on the partonic, especially gluonic, structure of the real photon from the resolved contribution of the cross section. Furthermore, the interplay between the hadronic and the point-like part of the real photon structure function can be studied.

As is well known, only qualitative conclusions can be drawn from LO calculations, since the results strongly depend on the factorization scale, especially in the resolved contribution. Furthermore, no dependence on jet definitions, present in the experimental data, can be seen in the LO results. Only the NLO cross sections, which contain an additional parton in the final state, depend on the jet definition. The NLO QCD corrections to the QPM diagram, i.e., the $\mathcal{O}(\alpha^2\alpha_s)$ contributions, consist of the radiation of a gluon in the final state and of the virtual corrections. The quark-antiquark pair emitted from the real photon can produce a collinear singularity in the real corrections, which has to be factorized and absorbed into the real photon structure function. In this way, the direct and resolved contributions achieve a dependence on the factorization scale M_γ. Thus the direct and resolved cross sections are not independent from each other in NLO QCD and the clear distinction mentioned above for the LO case does no longer hold. The NLO corrections to the subprocesses of the resolved contribution are equal to those obtained in deep inelastic *ep*-scattering, where the photon interacts directly with the partons from the proton. The singularities in the resolved contribution that do not cancel after adding the real and the virtual corrections are absorbed into the photon structure function, as for the direct case. In this paper we will concentrate on the calculation of the $\mathcal{O}(\alpha^2\alpha_s)$ terms in the direct part of the cross section for both, the transverse and the longitudinal polarization of the virtual photon. For separating the singular phase-space regions we apply the phase-space slicing method [15]. The resolved contributions are taken from the *ep*-scattering case, which has been calculated using the phase-space slicing method in [16, 17].

The paper is set out as follows. In section 2 we discuss cross sections in deep inelastic $e\gamma$ scattering in general and review the LO cross sections. We proceed in section 3 by performing the NLO calculation of the direct contribution for both polarizations of the virtual photon. The techniques for doing the calculations follow essentially those layed out in [5, 17, 18]. Some results for inclusive single- and dijet cross sections are presented in section 4 for kinematic conditions and energies encountered at LEP1 and LEP2. Section 5 contains the summary and an outlook. The results of the analytic calculations are presented in the appendix.

2 Leading Order Cross Sections

2.1 General Structure of the Cross Sections

To fix the notation we start by writing down the process of jet production in e^+e^- scattering:

$$e^+(k_a) + e^-(k_b) \longrightarrow e^+(k_a') + e^-(k_b') + \text{Jets} + \text{X} \quad . \tag{1}$$

We are interested in the case where one lepton radiates a virtual and the other a real photon. Of course, it does not matter which of the leptons radiates the virtual photon, but for definiteness we suppose this to be the positron. Thus, the subprocess we have to consider is $\gamma_a^*(q_a) + \gamma_b(q_b) \to \text{Jets} + \text{X}$, with $q_a = k_a - k_a'$, $q_b = k_b - k_b'$ and the virtualities $Q^2 = -q_a^2$ and $P^2 = -q_b^2 = 0$. The electron-positron center-of-mass (c.m.) energy is $s_H = (k_a + k_b)^2$. The hadronic, i.e., $\gamma^*\gamma$, c.m. energy is $W^2 = (q_a + q_b)^2$. Furthermore we define the variables

$$y_a = \frac{q_a k_b}{k_a k_b} \qquad \text{and} \qquad y_b = \frac{q_b k_a}{k_a k_b} \simeq 1 - \frac{E_e'}{E_e} \quad , \tag{2}$$

where E_e and E_e' are the energies of the incoming and outgoing electron in the e^+e^- center-of-mass system (c.m.s.), respectively. The variable y_b gives the momentum fraction of the real photon in the electron.

The cross section $d\sigma_{e^+e^-}$ for the process described above is given by the convolution

$$d\sigma_{e^+e^-} = \sum_k \int dx_b dy_b \; d\sigma_{e^+k} \; f_{k/\gamma}(x_b) \; F_{\gamma/e^-}(y_b) \quad . \tag{3}$$

Here, $F_{\gamma/e^-}(y_b)$ describes the spectrum of the real photons emitted from the electron according to the Weizsäcker-Williams approximation [19], which in its' simplest form reads

$$F_{\gamma/e^-}(y_b) = \frac{\alpha}{2\pi} \frac{1 + (1 - y_b)^2}{y_b} \ln\left(\frac{E_e^2 \theta_{max}^2}{m_e^2}\right) \quad . \tag{4}$$

The electron mass is m_e and θ_{max} is the maximum scattering angle of the electron. The function $f_{k/\gamma}(x_b)$ is the parton distribution function (PDF) of the real photon which describes the probability to find a parton with momentum $p_b = x_b q_b$ inside the real photon, where $x_b \in [0, 1]$. The direct process is included in formula (3) by viewing the photon as a parton with momentum fraction $x_b = 1$. It is obtained by summing not only over the quark flavors and the gluon, but also over the photon with $f_{\gamma/\gamma}(x_b) = \delta(1 - x_b)$. Last, $d\sigma_{e^+k}$ gives the positron-parton cross section, which is given by

$$d\sigma_{e^+k} = \frac{1}{4 s_H x_b y_b} \frac{4\pi\alpha}{Q^4} L_{\mu\nu} H^{\mu\nu} dL d\text{PS}^{(n)} \quad , \tag{5}$$

where $L_{\mu\nu} = 4(k_{a\mu} k'_{a\nu} - k'_{a\mu} k_{a\nu} - g_{\mu\nu} k_a k'_a)$ is the lepton tensor of the positron. In the resolved case, $H^{\mu\nu}$ is the hadron tensor familiar from deep-inelastic ep-scattering. In the direct case, $H^{\mu\nu}$ stands for the appropriate tensor describing the photon-photon scattering amplitudes (for a definition see e.g. [9, 20]). Note, that the lepton tensor of the electron radiating the real photon integrated over the azimuthal and polar angle of the outgoing electron gives the Weizsäcker-Williams formula (4). The n-particle phase space of the final state particles of the subprocess is $d\text{PS}^{(n)}$ and the positron phase space is given by

$$dL = \frac{Q^2}{16\pi^2} \frac{d\phi}{2\pi} \frac{dy_a dQ^2}{Q^2} \quad . \tag{6}$$

The azimuthal angle of the outgoing positron, ϕ, can be integrated out in the hadronic c.m.s. Using the definitions of the trace part of the hadron tensor $H_g = -g^{\mu\nu}H_{\mu\nu}$ (denoted by *g-part* in the following), the longitudinal part $H_L = (4Q^2)/(s_H y_a x_b)^2 p_b^\mu p_b^\nu H_{\mu\nu}$ and the unpolarized part $H_U = \frac{1}{2}(H_g + H_L)$, we find

$$\begin{aligned} \frac{1}{4Q^2}\int \frac{d\phi}{2\pi} L_{\mu\nu}H^{\mu\nu} &= \frac{1+(1-y_a)^2}{2y_a^2}H_g + \frac{4(1-y_a)+1+(1-y_a)^2}{2y_a^2}H_L \\ &= \frac{1+(1-y_a)^2}{y_a^2}H_U + \frac{2(1-y_a)}{y_a^2}H_L \quad . \end{aligned} \tag{7}$$

The expression H_U is used here to rewrite the result in a form familiar from DIS in ep-collisions. It should be noted that the real photon is unpolarized. The longitudinal cross section of the real photon is proportional to P^2 and vanishes since $P^2 = 0$.

2.2 Results in Leading Order

The LO cross sections are (per definition) finite. However, we will use dimensional regularization for the NLO corrections and thus we state also the LO results in $d = 4 - 2\epsilon$ space-time dimensions. We will neglect all quark masses in the following.

The Born approximation for the production of two final state quarks in the direct process is given by the process $\gamma^*\gamma \to q\bar{q}$. The resolved gluon and quark initiated subprocesses $\gamma^* q \to qg$ and $\gamma^* g \to q\bar{q}$ can be found e.g. in [17]. Note that the photon induced process $\gamma^*\gamma \to q\bar{q}$ is very similar to the one where the real photon is replaced by a gluon. The photon induced cross section can be obtained from the gluon induced one by keeping only the Abelian terms and setting $N_C = 1$ (hence $C_F = 0$) for the virtual photon vertex. In this way also the NLO corrections can be deduced.

Using the usual definitions of the Mandelstam variables $s = (p_b + q_a)^2$, $t = (p_b - p_1)^2$ and $u = (p_b - p_2)^2$, where p_1 and p_2 are the momenta of the final state particles, the two-body phase space reads

$$d\mathrm{PS}^{(2)} = \frac{1}{\Gamma(1-\epsilon)}\left(\frac{4\pi(s+Q^2)^2}{stu}\right)^\epsilon \frac{1}{(s+Q^2)}\,\frac{dt}{8\pi} \quad . \tag{8}$$

The matrix elements for the QPM process $\gamma^*\gamma \to q\bar{q}$ read

$$H^B_{g,L}(\gamma^*\gamma \to q\bar{q}) = 32\alpha^2\pi^2 Q_i^4 N_C\; T^\gamma_{g,L}(s,t,u) \quad . \tag{9}$$

For the gluon induced resolved matrix elements one finds

$$H^B_{g,L}(\gamma^* g \to q\bar{q}) = 16\alpha\alpha_s\pi^2 Q_i^2\; T^g_{g,L}(s,t,u) \quad , \tag{10}$$

whereas the quark initiated resolved matrix elements are given by

$$H^B_{g,L}(\gamma^* q \to qg) = 32\alpha\alpha_s\pi^2 Q_i^2 C_F\; T^q_{g,L}(s,t,u) \quad . \tag{11}$$

The definitions of $T^\gamma_{g,L}, T^g_{g,L}$ and $T^q_{g,L}$ can be found in Tab. 1.

Table 1: Definition of the LO matrix elements $T^{\gamma}_{g,L}, T^{g}_{g,L}$ and $T^{q}_{g,L}$ in terms of T_1, T_2 and T_3, defined in the appendix.

	photon induced	gluon induced	quark induced
g-part	$T^{\gamma}_{g}(s,t,u) = T_1(s,t,u)$	$T^{g}_{g}(s,t,u) = T_1(s,t,u)$	$T^{q}_{g} = -T_1(u,t,s)$
longitudinal part	$T^{\gamma}_{L}(s,t,u) = T_3(s,t,u)$	$T^{g}_{L}(s,t,u) = T_3(s,t,u)$	$T^{q}_{L} = T_2(s,t,u)$

3 Next-to-Leading Order Cross Sections

The NLO corrections are calculated with the help of dimensional regularization. The ultraviolet singularities in the one-loop contributions are regularized and subtracted in the modified minimal subtraction ($\overline{\rm MS}$) scheme. The infrared and collinear singularities from the real corrections are likewise calculated in dimensional regularization.

The $\mathcal{O}(\alpha_s)$ perturbative QCD corrections to the direct Born process $\gamma^*\gamma \to q\bar{q}$ are given by the gluon bremsstrahlung process $\gamma^*\gamma \to q\bar{q}g$ (see Fig. 2, upper row) and by the one-loop contributions to this process (see Fig. 2, lower two rows). The NLO corrections to the resolved processes constitute the one-loop contributions to the Born terms of section 2.2 and the four three-body contributions

$$\begin{aligned} \gamma^* g \to q\bar{q}g \quad &, \quad \gamma^* q \to qgg \quad , \\ \gamma^* q \to qq\bar{q} \quad &, \quad \gamma^* q \to qq'\bar{q}' \quad . \end{aligned}$$

The NLO resolved parton cross sections are of order $\alpha\alpha_s^2$, but, after they have been folded with the PDF's of the real photon, of the same order as the NLO direct cross sections [14]. In the following subsections we will consider only the direct part in some detail. The NLO resolved matrix elements are taken from Graudenz [17].

3.1 Virtual Corrections up to $\mathcal{O}(\alpha^2\alpha_s)$

We deduce the virtual correction to $\gamma^*\gamma \to q\bar{q}$ as mentioned above by keeping the Abelian term of the corresponding gluon induced process in order $\alpha\alpha_s^2$ and adjusting the color factors and the coupling. The one-loop process $\gamma^* g \to q\bar{q}$ can be calculated by crossing from the well-known one-loop corrections in $e^+e^- \to q\bar{q}g$ [21, 22], which has been done in [17].

Following the above procedure we obtain the results for the g-part and the longitudinal part:

$$H^{V}_{g,L}(\gamma^*\gamma \to q\bar{q}) = \frac{\alpha_s}{2\pi}\frac{\Gamma(1-\epsilon)}{\Gamma(1-2\epsilon)}\left(\frac{4\pi\mu^2}{Q^2}\right)^{\epsilon} (4\pi\alpha Q_i^2)^2 \; 2N_C C_F \; V_{g,L}(s,t,u) \quad . \tag{12}$$

The expressions V_g and V_L are stated in the appendix. The two-body phase-space is again given by eqn (8).

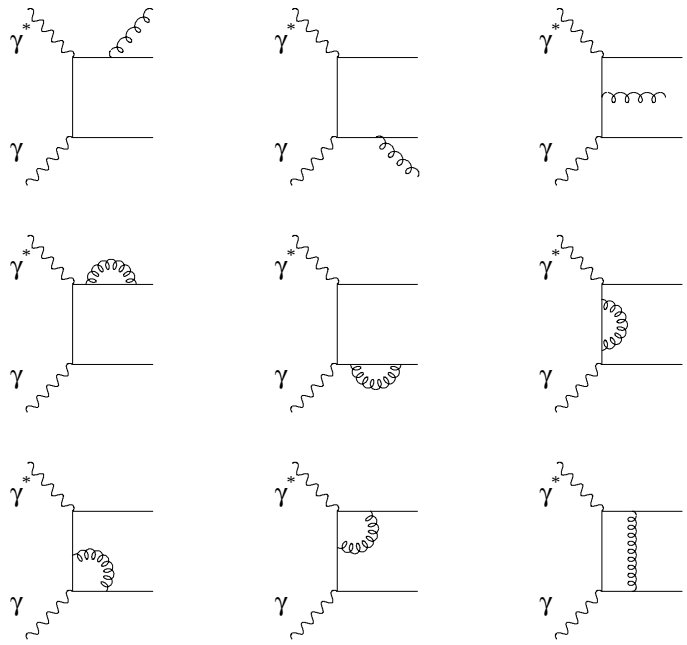

Figure 2: The $\mathcal{O}(\alpha_s)$ corrections to the QPM diagram of Fig. 1. Upper row: real gluon emission. Lower two rows: virtual corrections. Additional graphs are obtained by $s \to u$ crossing.

3.2 Real Corrections up to $\mathcal{O}(\alpha^2\alpha_s)$

The real corrections from the gluon bremsstrahlung process contain singular regions of phase-space that lead to two classes of singularities after integration. The final state gluon can become soft or collinear to one of the other final state particles, which will produce a final state singularity. Due to the on-shellness of the real initial state photon, the splitting term $\gamma \to q\bar{q}$ will produce an initial state singularity.

The method used here for handling these regions is the phase-space-slicing method [15], where a cut-off y_s is introduced in the phase-space integration to separate finite and singular regions. The finite integrals are handled numerically which opens the opportunity to introduce experimental cuts and jet definitions in a flexible way. The singular integrals are done analytically in $d = 4 - 2\epsilon$ dimensions. Both, the analytical and the numerical contributions will depend on the slicing parameter. Since y_s is a non-physical parameter the dependence of these parts on y_s should cancel in the sum. We will show this explicitly for our results later on.

After adding the $\mathcal{O}(\alpha^2\alpha_s)$ terms only single poles proportional to the photon splitting function $P_{q\leftarrow\gamma}$ will remain. These are absorbed into the photon structure function. We now handle the final and initial state singularities separately.

3.2.1 Final State Corrections

We consider the gluon bremsstrahlung process

$$\gamma^*(q_a) + \gamma(q_b) \to q(p_1) + \bar{q}(p_2) + g(p_3) \tag{13}$$

and concentrate on the case, where e.g. the invariant $r = (p_2 p_3)/(q_a q_b)$ vanishes and produces a singularity. The case $p_1 p_3 \to 0$ can be obtained by simply substituting $p_2 \to p_1$.

The analytical integration of the three body contributions H_g and H_L for the process (13) over $d\mathrm{PS}^{(3)}$ in the singular phase-space region is done by separating the three-particle phase-space into the two-particle phase-space $d\mathrm{PS}^{(2)}$ and a singular phase-space $d\mathrm{PS}^{(r)}$. In the c.m.s. of the final state particles p_2 and p_3 we define the variable $b = \frac{1}{2}(1 - \cos\theta)$, where θ is the angle between q_a and p_3, and $z = (q_a p_3)/(q_a q_b)$. Furthermore, ϕ defines the angle between the two planes defined by the particles $\{p_2, p_3\}$ and $\{p_1, q_b\}$. We define the variables

$$\tilde{s} = s = (q_a + q_b)^2, \qquad \tilde{t} = (q_b - p_1)^2, \qquad \tilde{u} = (q_b - p_2 - p_3)^2 - 2p_2 p_3 \tag{14}$$

from the three-body momenta. For $r \to 0$ the separation of the phase-space is given by $d\mathrm{PS}^{(3)} = d\mathrm{PS}^{(r)} d\mathrm{PS}^{(2)}$ with [5, 13, 17, 18]

$$d\mathrm{PS}^{(r)} = \frac{\Gamma(1-\epsilon)}{\Gamma(2-2\epsilon)} \frac{d\phi}{N_\phi} \sin^{-2\epsilon}\phi \left(\frac{4\pi}{s}\right)^\epsilon \frac{s}{16\pi^2} G_F(r) dr r^{-\epsilon} \frac{db}{N_b} [b(1-b)]^{-\epsilon} \tag{15}$$

with the function

$$G_F(r) = \left[1 - \frac{r}{(1-z)}\right]^{-\epsilon} = 1 + \mathcal{O}(r) \tag{16}$$

and the normalization constants

$$N_b = \int_0^1 db [b(1-b)]^{-\epsilon} = \frac{\Gamma^2(1-\epsilon)}{\Gamma(2-2\epsilon)}, \qquad N_\phi = \int_0^\pi d\phi \sin^{-2\epsilon}\phi = \frac{4^\epsilon \pi \Gamma(1-2\epsilon)}{\Gamma^2(1-\epsilon)} \quad . \tag{17}$$

The two-body phase-space $d\mathrm{PS}^{(2)}$ is once again given by eqn (8). Defining the variable $y_F = \min[-t/(s+Q^2), y_s]$, the limits of integration in $d\mathrm{PS}^{(r)}$ are given by $r \in [0, y_F]$, $b \in [0,1]$ and $\phi \in [0, \pi]$.

Expressing the $2 \to 3$ matrix elements H_g and H_L by the variables $\tilde{s}, \tilde{t}, \tilde{u}, r, b$ and ϕ in the limit $r \to 0$, we obtain the approximated matrix elements H_g^F and H_L^F. These are then integrated over the singular region of phase-space:

$$\int d\mathrm{PS}^{(r)} H_{g,L}^F = \frac{\alpha_s}{2\pi} \frac{\Gamma(1-\epsilon)}{\Gamma(1-2\epsilon)} \left(\frac{4\pi\mu^2}{Q^2}\right)^\epsilon (4\pi\alpha Q_i^2)^2 \, 2N_C C_F \, F_{g,L} \quad . \tag{18}$$

The final results for F_g and F_L are listed in the appendix. They contain the IR collinear and soft singularities that cancel against those of the virtual corrections. It is essential that the singular terms are proportional to the LO matrix elements and that $\tilde{s}, \tilde{t}$ and $\tilde{u}$ reduce to the usual two-body invariants s, t and u for the above limit $r \to 0$.

3.2.2 Photon Initial State Corrections

In the direct case the real photon can split into a $q\bar{q}$ pair that gives rise to a collinear singularity if the partons are emitted parallel. The singularity appears when the invariant $z_1 = (q_b p_1)/(q_a q_b)$ vanishes. We define the new variable

$$z_b = \frac{(p_2 p_3)}{(q_a q_b)} \in [\eta_b, 1] \quad , \tag{19}$$

that gives the fraction of the momentum q_b that participates in the subprocess after a particle has been radiated in the initial state. The variable $\eta_b \in [0,1]$ is connected to z_b through $\eta_b = x_b z_b$. Furthermore, we define the invariants

$$\tilde{s} = (p_2 + p_3)^2, \qquad \tilde{t} = (z_b q_b - p_2)^2, \qquad \tilde{u} = (z_b q_b - p_3)^2 \tag{20}$$

from the three-body momenta. All other definitions concerning the phase-space slicing remain as in the previous subsection. In the limit $z_1 \to 0$ the variable $\tilde{s}$ reduces to s. In the same limit the three-body phase-space separates according to $d\mathrm{PS}^{(3)} = d\mathrm{PS}^{(2)} d\mathrm{PS}^{(r)}$, where [13]

$$\begin{aligned} d\mathrm{PS}^{(r)} &= \frac{1}{\Gamma(1-\epsilon)} \frac{d\phi}{N_\phi} \sin^{-2\epsilon}\phi \left(\frac{4\pi}{s}\right)^{\epsilon} \frac{s}{16\pi^2} G_I(z_1) \\ &\times dz_1 z_1^{-\epsilon} \frac{dz_b}{z_b} \left(\frac{1-z_b}{z_b} - \frac{Q^2}{s}\right)^{-\epsilon} \left(1 + \frac{Q^2(1-z_b)}{z_b(z_b s - (1-z_b)Q^2)}\right)^{1-\epsilon} \end{aligned} \tag{21}$$

with

$$G_I(z_1) = \left[1 - z_1 \frac{s - z_b Q^2}{s(1-z_b) - z_b Q^2}\right]^{-\epsilon} = 1 + \mathcal{O}(z_1) \quad . \tag{22}$$

The two-body phase-space is given by equation (8). The integration over $d\mathrm{PS}^{(r)}$ with $z_1 \in [0, -u/(s+Q^2)]$, $z_b \in [\eta_b, 1]$ and $\phi \in [0, \pi]$ is restricted to the singular region of z_1 in the range $z_1 \in [0, y_I]$ with $y_I = \min[-u/(s+Q^2), y_s]$.

Expressing the matrix elements H_g and H_L with the variables $\tilde{s}, \tilde{t}, \tilde{u}, z_1, z_b, b$ and ϕ and taking the limit $z_1 \to 0$, one obtains the approximated matrix elements H_g^I and H_L^I. These are integrated according to

$$\int d\mathrm{PS}^{(r)} H_{g,L}^I = \frac{\alpha_s}{2\pi} \frac{\Gamma(1-\epsilon)}{\Gamma(1-2\epsilon)} \left(\frac{4\pi\mu^2}{Q^2}\right)^{\epsilon} (4\pi\alpha Q_i^2)^2 \, 2N_C C_F \int_{\eta_b}^{1} \frac{dz_b}{z_b} I_{g,L} \quad , \tag{23}$$

where I_g and I_L are stated in the appendix.

3.3 Finite Next-to-Leading Order Cross Section

The full NLO cross section $d\sigma_{e^+e^-}^{NLO}$ can be written as a sum of the y_s-dependent two- and three-body cross sections $d\sigma_2$ and $d\sigma_3$:

$$d\sigma_{e^+e^-}^{NLO} = d\sigma_2(y_s) + d\sigma_3(y_s) \quad . \tag{24}$$

The y_s-dependence in $d\sigma^{NLO}_{e^+e^-}$ cancels up to terms of order $y_s \ln^n y_s$ which have been neglected in the analytical calculations. Thus, y_s has to be chosen sufficiently small for the approximations to be valid. The two-body cross section consists of the final state, virtual, initial state and Born contributions $d\sigma^F$, $d\sigma^V$, $d\sigma^I$ and $d\sigma^B$:

$$d\sigma_2(y_s) = d\sigma^F(y_s) + d\sigma^V + d\sigma^I(y_s) + d\sigma^B \quad . \tag{25}$$

When the virtual and final state cross sections are added, the pole terms cancel, as can be seen by directly comparing formulæ (40) and (41) with (42) from the appendix. The simple pole appearing in the initial state singularities I_g and I_L is proportional to the splitting function $P_{q\leftarrow\gamma}(z_b)$. This function appears in the evolution equation of the PDF of the real photon as an inhomogeneous (point-like) term. Therefore, the photon initial state singularities can be absorbed into the real photon PDF, according to the procedure given in [23, 18]. We define the renormalized PDF f_{q/e^-} of a quark q in the electron as

$$f_{q/e^-}(\eta_b, M_\gamma^2) = \int_{\eta_b}^1 \frac{dz_b}{z_b} \left(\delta_{q\gamma}\delta(1-z_b) + \frac{\alpha_s}{2\pi}\Gamma^{(1)}_{q\leftarrow\gamma}(z_b, M_\gamma^2) \right) f_{\gamma/e^-}\left(\frac{\eta_b}{z_b}\right) \quad , \tag{26}$$

where f_{γ/e^-} is the LO PDF before the absorption of the collinear singularity. The NLO transition function is given by

$$\Gamma^{(1)}_{q\leftarrow\gamma}(z_b, M_\gamma^2) = -\frac{1}{\epsilon} P_{q\leftarrow\gamma}(z_b) \frac{\Gamma(1-\epsilon)}{\Gamma(1-2\epsilon)} \left(\frac{4\pi\mu^2}{M_\gamma^2}\right)^\epsilon + C_{q/\gamma}(z_b) \tag{27}$$

with $C_{q/\gamma}(z_b) \equiv 0$ in the $\overline{\text{MS}}$ scheme. In the discussed order, $P_{g\leftarrow\gamma}(z_b) = 0$. The initial state contribution $d\sigma^I(\gamma^*\gamma \to \text{jets})$ for the photon initial state singularity is calculated from the unrenormalized cross section $d\bar{\sigma}$ by

$$d\sigma^I(\gamma^*\gamma \to \text{jets}) = d\bar{\sigma}(\gamma^*\gamma \to \text{jets}) - \frac{\alpha_s}{2\pi} \int dz_b \Gamma^{(1)}_{q\leftarrow\gamma}(z_b, M_\gamma^2) d\sigma^B(\gamma^* q \to \text{jets}) \quad . \tag{28}$$

The cross section $d\sigma^B$ contains the LO photon-parton scattering matrix elements given in section 2, $H^B_{g,L}(\gamma^* q \to qg)$. The factor $(4\pi\mu^2/M_\gamma^2)^\epsilon$ in eqn (27) is combined with the factor $(4\pi\mu^2/Q^2)^\epsilon$ in eqn (23) and leads to a factorization scale dependent term of the form

$$-\frac{1}{\epsilon} P_{q\leftarrow\gamma}(z_b) \left[\left(\frac{4\pi\mu^2}{Q^2}\right)^\epsilon - \left(\frac{4\pi\mu^2}{M_\gamma^2}\right)^\epsilon \right] = -P_{q\leftarrow\gamma}(z_b) \ln\left(\frac{M_\gamma^2}{Q^2}\right) + \mathcal{O}(\epsilon) \quad . \tag{29}$$

In this way, the subtracted partonic cross section will depend on the scale M_γ^2, as does the PDF of the resolved photon.

After this subtraction procedure, all terms in the two-body cross section $d\sigma_2$ are finite and the limit $\epsilon \to 0$ can be performed. Eqn (24) then yields a physically meaningful cross section.

4 Numerical Results

We now come to a discussion of numerical results for single- and dijet inclusive jet cross sections. Before analyzing these physical cross sections, we discuss some checks of the analytical results, one being the dependence of the cross sections on the phase-space slicing parameter y_s. Furthermore we show the dependence of the cross sections on the factorization scale. The multi-dimensional integrals are performed using the VEGAS [24] Monte Carlo integration routine.

At LEP, electrons are scattered on positrons with equal energy. Events are selected in a certain angular range of the tag and rejected if there is also an antitag above a certain energy and scattering angle. This corresponds to the situation, where one photon is quasi-real and the other has a finite, non-vanishing virtuality.

In this paper we will give predictions at LEP1 and LEP2 energies for certain characteristic values of the photon virtuality Q^2, namely $Q^2 = 10, 20, 100$ and 200 GeV^2. At LEP1, the electron and the positron both have the energy $E_e = E_p = 45.5$ GeV, corresponding to a c.m.s. energy of $\sqrt{s} = 91$ GeV. The energies of the two incoming leptons at LEP2 are $E_e = E_p = 91.5$ GeV, giving a c.m.s. energy of $\sqrt{s} = 183$ GeV. The antitag conditions are taken into account by using the Weizsäcker-Williams formula (4) with $\theta_{max} = 25$ milliradians in the case of LEP1 and with $\theta_{max} = 33$ milliradians for LEP2. We have not imposed cuts on y_a and y_b, i.e., $y_a, y_b \in [0, 1]$. We will calculate the cross sections in the hadronic ($\gamma^*\gamma$) c.m.s. For the theoretical studies here we will refrain from taking into account the exact tagging conditions from the LEP experiments [11] and will concentrate on the above stated energies, although also higher energies will become available at LEP2.

The jets are clustered at LEP using the Snowmass cone algorithm [25], where hadrons i are combined into a single jet, if their distance from the jet center in azimuth-rapidity space, given by

$$R_{i,J} = \sqrt{(\eta_i - \eta_J)^2 + (\phi_i - \phi_J)^2} \quad , \tag{30}$$

is smaller than a cone radius R, i.e., for $R_{iJ} \leq R$. Here, η_J and ϕ_J are the rapidity and the azimuthal angle of the combined jet respectively, defined as

$$E_{T_J} = E_{T_1} + E_{T_2} \tag{31}$$

$$\eta_J = \frac{E_{T_1}\eta_1 + E_{T_2}\eta_2}{E_{T_J}} \quad , \tag{32}$$

$$\phi_J = \frac{E_{T_1}\phi_1 + E_{T_2}\phi_2}{E_{T_J}} \quad . \tag{33}$$

The radius R is chosen as in the experimental analysis, namely $R = 1$.

For the parton densities of the photon we use the NLO parametrization of Glück, Reya and Vogt [26], transformed from the DIS$_\gamma$ to the $\overline{\text{MS}}$ scheme. The corresponding Λ value is $\Lambda^{(4)} = 200$ MeV. Since the energies are quite large, we will choose $N_F = 5$ flavors for our computations. The renormalization and factorization scales are set equal to Q. In particular for the larger values of Q^2 this is a slightly better choice than E_T, since the minimum transverse energy of $E_{T_{min}} = 3$ GeV is rather small. We could have

chosen E_T as a scale, especially for the E_T-spectra, but we prefered to take one scale consistently throughout the work. The choice of scale only has a marginal effect on the results presented in the next sections.

4.1 Check of the Analytical Results

From section 3.3 it is already clear that the poles encountered in the real corrections cancel against those from the virtual corrections, which is a test of the singular terms in the NLO corrections. The remaining photon initial state singularities have been absorbed into the structure function of the real photon. As a further test we have checked that the analytic formulæ given in the appendix reduce to the expressions encountered in $\gamma\gamma$ scattering (photoproduction limit, i.e., $Q^2 \to 0$) stated in [5].

A test of the y_s dependent terms is the calculation of the two-body and three-body cross sections as a function of y_s. The dependence should cancel in the sum of the two contributions. In the analytical calculation, terms of order $y_s \ln^n y_s$ have been omitted and thus the slicing parameter, which is normalized with the hadronic c.m.s. energy, has to be chosen much smaller than one. In Fig. 3 a and b we show the single inclusive direct jet cross section integrated over $E_T > 3$ GeV as a function of y_s, integrated over the two different Q^2-regions $Q^2 \in [10, 20]$ GeV^2 and $Q^2 \in [100, 200]$ GeV^2 for the above stated LEP1 conditions. The analytic two-body contributions (dashed) are negative and the absolute value is quite large for the smaller values of y_s. The three-body contributions (dotted) are large and positive. The sum of these (full) is independent of the slicing parameter in the shown region of y_s, as expected. Although it is theoretically safer to choose smaller values of y_s, because of the omission of the $\mathcal{O}(y_s)$-terms, it is from the practical (numerical) point of view convenient to have larger values of y_s, since the compensation between the two-body and the three-body parts are then smaller and the statistical errors are likewise smaller. We will choose $y_s = 5 \cdot 10^{-3}$ in the further calculations.

In Fig. 3 we also compare the NLO cross section with the LO result (the dash-dotted line), which does not depend on y_s. For the LO cross sections we have chosen the same two-loop α_s formula and the same PDF as in the NLO cross sections, so differences between the LO and NLO results are due to differences in the LO and NLO matrix elements. The NLO curves are smaller than the LO order ones and the corrections are around 10% for the smaller Q^2 region. For the larger Q^2 region the NLO corrections reduce the Born result by approximately 30%.

The resolved contributions are also independent of y_s, which we explicitly checked but do not show here. Similar tests of the resolved contribution have already been performed for the case where the real photon is substituted by a proton in [13].

4.2 Scale-Dependences

Having checked the pole terms, the limiting behavior and the y_s-independence, which shows that the program for the numerical calculations is reliable, we proceed by discussing the dependences of the cross sections on the renormalization- and factorization-scales in

LO and NLO. This has been done before in the limiting case of $Q^2 \to 0$, i.e., for $\gamma\gamma$-scattering, in [6].

In Fig. 4 a and b we show the variation of the NLO direct and LO resolved cross sections with the factorization scale M_γ (normalized with Q) for the same kinematic conditions and regions of virtuality as in Fig. 3. In both regions, the LO resolved cross section (dotted line) grows by about 50%, going from $M_\gamma = \frac{1}{2}Q$ to $M_\gamma = 2Q$. This dependence is due to the factorization scale dependence of the photon structure function alone, since the LO partonic cross sections are finite and no initial state singularities have to be treated. The dependence of the LO resolved contribution is completely canceled by the NLO direct contribution, shown as the dashed line. The sum (full line) shows no dependence on the factorization scale in the plotted region. The dependence of the NLO direct contribution on the factorization scales comes in through the absorption of the singular terms in the initial state into the photon structure function, as explained in section 3.3. The resolved NLO corrections to the partonic cross section do depend on the factorization scale, in contrast to the resolved LO partonic cross sections. One sees however only a small overall dependence on the factorization scale of under 4% by going from $M_\gamma = \frac{1}{2}Q$ to $M_\gamma = 2Q$, when the NLO direct and resolved contributions are added to obtain the full NLO cross section (we do not show these plots here).

The renormalization scale dependence of the resolved cross section is reduced by going from LO to NLO, as has been shown in [13]. For the direct cross section, the LO result is independent of the renormalization scale, because the strong coupling constant α_s does not appear in the QPM diagram. Thus, the NLO cross section is actually LO in the strong coupling. As we will see later on, the NLO correction to the LO direct process is small and thus the renormalization scale dependence, which is only seen in the NLO corrections, will likewise be small. In addition, the running of the strong coupling is compensated by including the virtual graphs in the NLO direct process. We found only a small variation of the NLO direct cross section of about 10% between the smallest and largest scale considered here. Thus, summing the direct and resolved contributions we find a reduced renormalization scale dependence due to the reduced dependence of the resolved components.

4.3 Inclusive Single-jet Cross Sections

We start this section by discussing the single-jet inclusive η-distributions

$$\frac{d\sigma^{1jet}}{d\eta dQ^2} = \int dE_T \frac{d\sigma^{1jet}}{dE_T dQ^2 d\eta} \tag{34}$$

in the region $|\eta| < 3$, integrated over $E_T > 3$ GeV for LEP1 conditions. We show the direct and resolved cross sections and their sum in Fig. 5 and look at the longitudinal and transverse contributions to the individual direct and resolved components in Fig. 6 and Fig. 7.

Fig. 5 a,b,c and d show the direct (dashed) and resolved (dotted) contributions as well as their sum (full line) for the four Q^2 values defined above, $Q^2 = 10, 20, 100$ and

200 GeV^2. The direct contributions are peaked at $\eta = 0$ and are quite symmetric, which is to be expected, since we are in the $\gamma^*\gamma$ c.m.s. A small asymmetry arises from the mass of the virtual photon. The resolved cross section is peaked at $\eta = 0.5$ and shows a stronger asymmetry. This is due to the additional integration over the momentum fraction of the parton in the resolved photon. The peak is in the positive η-region, since the virtual photon is chosen to travel along the positive z-axis. Four all Q^2 values, the direct contribution is the dominant one, although the resolved becomes more important for larger Q^2 values and in general for positive η's. This shows that the direct contribution falls of slightly stronger with rising Q^2 compared to the resolved contribution. The reason for this is the relatively low cut on E_T, where the resolved component is expected to be more important.

In Fig. 6 a,b,c and d we show the direct cross section, split up into the transverse and longitudinal parts, compared to the full LO cross section. The transverse part (dashed line) is denoted by σ_T and is obtained from the full cross section by setting $H_L = 0$, so only the g-part is in σ_T. Likewise, the longitudinal part σ_L (dotted line) is obtained by setting $H_g = 0$. The sum of both gives the full direct contribution, denoted here as σ_D (full line). For the plots a and b, the transverse part is dominant, although the longitudinal part is important, especially in the central region. One observes a plateau around $\eta = 0$ for the transverse part, which becomes a dip for the two larger Q^2-values in Fig. 6 c and d. This local minimum is compensated in the full direct cross section σ_D through the longitudinal component which has a maximum around $\eta = 0$. From this one sees that the longitudinal polarization of the virtual photon gives an important contribution to the direct cross section. The NLO direct cross section σ_D is compared to the LO cross section (dash-dotted line), containing both polarizations of the virtual photon. In Fig. 6 a and b, the LO and NLO cross sections can not be distinguished in the logarithmic plot, but the NLO curves lie around 5-10% lower than the LO ones, which is consistent with the results shown Fig. 3. For the two larger Q^2-values, the NLO curve lies approximately 25% below the LO cross section in the central η-region. Furthermore, the NLO cross section has a slightly stronger fall-off towards the edges of the η phase space than the LO cross section.

The dip observed in the NLO transverse cross section is already present in LO, which we do not show here. It is not present in photoproduction and for the smaller Q^2 values. In LO the reason for the local minimum at larger Q^2 is twofold. First, the interference term in the Born matrix elements $-Q^2 s/(ut)$ is negative and sharpley centered around $\eta = 0$. For small Q^2 this contribution is negligable, but going to larger virtualities the subtraction of the interference term in the central η-region leads to the observed local minimum. Second, the individual terms t/u and u/t in the Born matrix elements are peaked on opposite sides, slightly away from $\eta = 0$. For $Q^2 = 0$ their sum still gives a curve with an absolute maximum at $\eta = 0$. At larger Q^2 values though the maxima of the terms t/u and u/t move to larger (smaller) η-values, so that their sum leads to a slight local minimum near $\eta = 0$. These effects, observed in LO, have their correspondences in NLO.

Next, we consider the resolved components, again separated into transverse and longitudinal parts, in Fig. 7 a,b,c and d. The curves are labeled as in Fig. 6. The transverse

part of the cross section is dominant for all Q^2 values and the longitudinal part even becomes less important for the larger virtualities and is one order of magnitude smaller compared to the transverse part at $Q^2 = 200$ GeV^2. The longitudinal part is peaked more in the positive η region for the smaller Q^2 values than the transverse part and it is shifted to the smaller η's for the larger Q^2 values. Here, also the LO curves and the NLO curves are not distinguishable in the logarithmic plots of Fig. 7 a and b. For the resolved cross section, the NLO cross sections are around 10% larger than the LO cross sections, in contrast to the direct case, where the NLO cross sections lie lower than the LO cross sections. It should be mentioned that the transverse part of the gluon induced resolved cross section also shows a dip near $\eta = 0$, for the same reasons as in the case of the transverse direct cross section. However, the gluon induced process gives only a rather small contribution to the resolved cross section and the transverse part of the quark induced cross section does not have a local minimum in the η-distribution, since here the interference term is positive.

In connection with the E_T-distributions it will turn out to be important that the direct cross sections have a larger plateau in the central η-region than the resolved components, which are peaked more sharply around $\eta = 0.5$ and fall off stronger towards the edges of the η phase space. The effect is stronger for the larger Q^2 values. This is due to the special form of the transverse direct cross section, which is relatively broad already for the smaller Q^2 values and has two maxima at the edges of the η spectrum for the larger Q^2 values. We further mention that the η distributions become narrower when integrated over $E_T > E_{T_{min}}$ for larger values of $E_{T_{min}}$ due to the stronger kinematical restrictions in the region of larger E_T. This holds for both, the direct and the resolved components.

We now come to the E_T distributions of the single-jet inclusive cross section

$$\frac{d\sigma^{1jet}}{dE_T dQ^2} = \int d\eta \frac{d\sigma^{1jet}}{dE_T dQ^2 d\eta} \tag{35}$$

for the same Q^2-values as in Fig. 5. The rapidity is integrated over the central region $|\eta| < 2$ in the hadronic c.m.s. We show the NLO distributions of the direct (dashed) and the resolved (dotted) component of the cross section and the sum (full line) of the two in the E_T-range $E_T \in [3, 11]$ GeV in Fig. 8 a,b,c and d.

As can be seen, the direct component is the dominant one in the whole E_T-range for the two smaller Q^2-values. In addition the resolved contribution falls off stronger with rising E_T than the direct component. The stronger fall-off of the resolved component holds for the two larger Q^2-values as well, but here the resolved component becomes comparable to the direct contribution for the smallest E_T values. The flattening of the E_T distribution of the direct component for the small E_T's, already visible at $Q^2 = 100$ GeV^2, even leads to a crossing of the direct and resolved cross sections at $E_T = 3$ GeV for the largest Q^2-value, Fig. 4d, so that the resolved is larger than the direct.

This behavior is a purely kinematical effect and stems from the fact that the η-integration is restricted to $|\eta| < 2$. We have mentioned above that the direct cross sections have a broader η-spectrum than the resolved ones. Cutting on η thus leads to a stronger cut on the direct than on the resolved components. The effect becomes more

important for the larger Q^2 values because the direct contributions have an even broader η-spectrum for $Q^2 = 100$ and 200 GeV^2 than for the smaller Q^2 values, as already discussed above. Since the η-spectra become narrower for the larger E_T's, the cut on η does no longer have such a large effect on the direct cross section and the direct component again dominates over the resolved component for the larger E_T's.

As a main result we find that the resolved contribution is small compared to the direct contribution and therefore there is little hope to learn about the parton distributions, especially the gluon distributions, in the photon from deep-inelastic $e\gamma$-scattering. Furthermore, the resolved component is largely suppressed for larger transverse energies E_T, which agrees with the expectation that the point-like part of the real photon is dominant at large scales.

4.4 Inclusive Dijet Cross Sections

We now come to the presentation of inclusive dijet cross sections for LEP1 and LEP2 energies. In Fig. 9 a,b,c and d we show the dijet cross section $d\sigma^{2jet}/dE_{T_1}dQ^2$ integrated over $\eta_1, \eta_2 \in [-2, 2]$ as a function of the transverse momentum of the trigger jet E_{T_1} for the same Q^2-values as in Fig. 5 (a)–(d) for LEP1 conditions. We see much the same behavior as in the case of the single-jet cross sections, namely that the direct component is dominant and the resolved one falls off stronger with rising E_T. As in the single-jet case, the direct cross section has a flattening towards the smaller E_T's for the largest Q^2 values, which seems to be even stronger in the two-jet case. The reasons for the flattening are the same as discussed above in the single-jet case, only here we have a cut on the η's of both jets, which increases the effect of the η-cuts and thus the flattening of the E_T distributions.

In Fig. 10 a,b,c and d the dijet cross section integrated over $\eta_1, \eta_2 \in [-2, 2]$ is shown in the range $E_T \in [3, 11]$ GeV for LEP2 conditions, i.e., for slightly different antitagging conditions than for LEP1 and for larger energies. Therefore, the cross sections are larger than for the dijet cross sections for LEP1. All other conclusions remain unchanged. The phenomenon of the flattening turns out to be quite obvious here. As can be seen in Fig. 10 d, the direct contribution even has a slight maximum in the E_T spectrum for $E_T = 4$ GeV and by going to smaller E_T values the direct cross section becomes smaller. This is compensated by the rise in the resolved component, so that the sum of the direct and the resolved component rises by going to smaller E_T's.

5 Summary and Outlook

We have presented the calculation of the direct component of jet production in deep inelastic electron-photon scattering in NLO QCD. Transverse and longitudinal polarizations of the virtual photon have been taken into account. The singular regions of phase space have been extracted with the help of the phase-space slicing method. The initial state singularities of the real photon have been absorbed into the PDF of the real photon. Cross

sections have been obtained by adding the direct and resolved real photon parts. The spectrum of the real photon has been approximated by the Weisäcker-Williams formula. We have shown that the scale dependence of the NLO cross sections are reduced. We are thus in the position to compare NLO calculations to experimental data for deep inelastic $e\gamma$ scattering, taken e.g. at LEP1 and LEP2.

We have presented η- and E_T-distributions of inclusive one- and two-jet cross sections for LEP1 and LEP2 energies for photon virtualities between 10 and 200 GeV^2. The direct component gives the dominant contribution to the cross section. The NLO direct cross sections are about 20% smaller than the LO cross sections for $Q^2 > 100$ GeV^2 and about the same size for Q^2 around 20 GeV^2. The longitudinal part of the cross section plays an important role and can contribute up to 50% in the full cross section.

It is of course possible to study the influence of different parametrizations of the real photon PDF on the resolved cross section. We have refrained from showing such comparisons here, because the resolved plays only a minor role in the cross sections. Furthermore it is possible to study the effects of cuts on other observables, such as $x_\gamma, \cos\theta^*$ or the invariant jet mass, in NLO, as has been done for $\gamma\gamma$-scattering in [6]. However, data on these kind of variables are not expected in the near future.

It has been discussed recently in [27] in connection with ep-scattering at HERA that contributions from the resolved virtual photon might contribute to jet cross sections up to virtualities of 100 GeV^2. The resolved virtual photon contributions have to be taken into account when terms of the type $\ln Q^2/E_T^2$ become large and have to be absorbed into a virtual photon structure function, as is the case for $Q^2 \ll E_T^2$. The subtraction procedure has been worked out in [28] for the case of ep-collisions and is very similar for $e\gamma$-reactions [13].

In this paper we have not taken into account the effects of a resolved virtual photon. However, the case of ep-scattering corresponds to the small resolved contribution in the $\gamma^*\gamma$ case. The resolved virtual photon effects in the direct cross section will presumably be small for larger Q^2 values and it is not clear how the double-resolved contribution, i.e., the contribution where the real and the virtual photons are both resolved, behaves. We will extend our studies presented here in the future to include the effects of resolved virtual photons.

Acknowledgments

I am grateful to G. Kramer for discussions and comments on the manuscript. I thank E. McKigney, D.J. Lauber and D. Miller for explaining to me some details of the LEP single-tag experiment.

Appendix

Born Terms and Virtual Corrections

The Mandelstam variables s, t and u, as well as the invariants Q^2, s_H, x_b and y_a are defined as in section 2 in the main part. The LO matrix elements in $d = 4-2\epsilon$ space-time dimensions are given by

$$T_1(s,t,u) = (1-\epsilon)\left(\frac{t}{u}+\frac{u}{t}\right) - \frac{2Q^2 s}{ut} - 2\epsilon \quad , \tag{36}$$

$$T_2(s,t,u) = -(1-\epsilon)\,\frac{4Q^2}{(s_H x_b y_a)^2}\,\frac{u}{2} \quad , \tag{37}$$

$$T_3(s,t,u) = \frac{4Q^2}{(s_H x_b y_a)^2}\,s \quad . \tag{38}$$

The one-loop contributions to the process $\gamma^*\gamma \to q\bar{q}$ depend on the two-body variables s, t and u. The function $L(x,y)$ appearing in the virtual corrections is defined as [17]

$$\begin{aligned} L(x,y) &= \ln\left|\frac{x}{Q^2}\right|\ln\left|\frac{y}{Q^2}\right| - \ln\left|\frac{x}{Q^2}\right|\ln\left|1-\frac{x}{Q^2}\right| - \ln\left|\frac{y}{Q^2}\right|\ln\left|1-\frac{y}{Q^2}\right| \\ &- \lim_{\eta\to 0}\mathrm{Re}\left[\mathcal{L}_2\left(\frac{x}{Q^2}+i\eta\right)+\mathcal{L}_2\left(\frac{y}{Q^2}+i\eta\right)\right] + \frac{\pi^2}{6} \quad , \end{aligned} \tag{39}$$

where $\mathcal{L}_2(x)$ is the Dilogarithm function. For the g-part of the virtual corrections we find

$$\begin{aligned} V_g(s,t,u) &= T_1(s,t,u)\left[-\frac{2}{\epsilon^2}-\frac{2}{\epsilon}\left(\frac{3}{2}-\ln\frac{s}{Q^2}\right)+\frac{2\pi^2}{3}-8-\ln^2\frac{s}{Q^2}\right] \\ &+ 4\ln\frac{s}{Q^2}\left(\frac{2s}{u+t}+\frac{s^2}{(u+t)^2}\right) \\ &+ \ln\frac{-u}{Q^2}\left(\frac{4s+2u}{s+t}-\frac{ut}{(s+t)^2}\right)+\ln\frac{-t}{Q^2}\left(\frac{4s+2t}{s+u}-\frac{ut}{(s+u)^2}\right) \\ &- 2L(-s,-u)\frac{s^2+(s+t)^2}{ut} - 2L(-s,-t)\frac{s^2+(s+u)^2}{ut} \\ &+ \left(\frac{4s}{u+t}+\frac{s}{u+s}+\frac{s}{s+t}\right)-\left(\frac{s}{u}+\frac{s}{t}+\frac{u}{t}+\frac{t}{u}\right) \quad . \end{aligned} \tag{40}$$

For the longitudinal part we find

$$\begin{aligned} V_L(s,t,u) &= T_3(s,t,u)\left[-\frac{2}{\epsilon^2}-\frac{2}{\epsilon}\left(\frac{3}{2}-\ln\frac{s}{Q^2}\right)+\frac{2\pi^2}{3}-8-\ln^2\frac{s}{Q^2}\right. \\ &+ \frac{1}{2}\ln\frac{-u}{Q^2}\left(\frac{2t}{s+t}+\frac{ut}{(s+t)^2}\right)+\frac{1}{2}\ln\frac{-t}{Q^2}\left(\frac{2u}{s+u}+\frac{ut}{(s+u)^2}\right) \\ &+ \left.-\frac{1}{2}\left(14+\frac{s}{s+u}+\frac{s}{s+t}\right)-L(-u,-s)-L(-t,-s)\right] \quad . \end{aligned} \tag{41}$$

Final State Corrections

The final state corrections to the process $\gamma^*\gamma \to q\bar{q}g$ depend on the invariant mass cut-off y_F and on s, t and u. Neglecting terms of order ϵ, we find

$$\begin{aligned} F_g(s,t,u) &= T_1(s,t,u)\left\{\frac{2}{\epsilon^2}+\frac{2}{\epsilon}\left(\frac{3}{2}-\ln\frac{s}{Q^2}\right)+7\right. \\ &- \left. 3\ln\frac{-y_F(t+u)}{Q^2}-2\ln^2\frac{-y_F(t+u)}{s}+\ln^2\frac{s}{Q^2}-\frac{2\pi^2}{3}\right\} \quad . \end{aligned} \tag{42}$$

The longitudinal correction in the final state, F_L, is simply obtained by replacing the Born term T_1 by T_3.

Photon Initial State Corrections

The photon initial state singularity depends on the cut-off parameter y_I, the additional variable of integration z_b and on s, t and u. Again, terms of order ϵ have been neglected:

$$\begin{aligned} I_g(s,t,u) &= -\frac{1}{2N_C}T_1(t,s,u)\left\{\left(-\frac{1}{\epsilon}-1\right)P_{q\leftarrow\gamma}(z_b)\right. \\ &+ \left.\left(\ln\frac{-y_I(t+u)}{Q^2}+\ln\frac{1-z_b}{z_b}\right)P_{q\leftarrow\gamma}(z_b)+N_C\right\} \quad . \end{aligned} \tag{43}$$

The longitudinal term, I_L, can be obtained by replacing the T_1 by T_3, as for the final state corrections, keeping the invariants t and s exchanged. The Altarelli-Parisi splitting function in (43) is given by

$$P_{q\leftarrow\gamma}(z) = N_C\left(z^2+(1-z)^2\right) \quad . \tag{44}$$

References

[1] H. Hayashi et al., TOPAZ Collaboration, Phys. Lett. **B314** (1993) 149; B.J. Kim et al., AMY Collaboration, Phys. Lett. **B325** (1994) 248.

[2] K. Ackerstaff et al., OPAL Collaboration, Z. Phys. **C73** (1997) 433.

[3] P. Aurenche, J.-Ph. Guillet, M. Fontannaz, Y. Shimizu, J. Fujimoto, K. Kato, Progr. Theor. Phys. **92** (1994) 175.

[4] L.E. Gordon, Nucl. Phys. **B419** (1994) 25.

[5] T. Kleinwort, G. Kramer, Nucl. Phys. **B477** (1996) 3;
M. Klasen, T. Kleinwort, G. Kramer, report DESY 97-234, EPJ direct 1 (1998) 1.

[6] T. Kleinwort, report DESY-96-165 (unpublished).

[7] T. Kleinwort, G. Kramer, Phys. Lett. **B370** (1996) 141; Z. Phys. **C75** (1997) 489.

[8] F.M. Renard, Z. Phys. **C14** (1982) 209.

[9] Ch. Berger, W. Wagner, Phys. Rep. **146** No. 1& 2 (1987) 1.

[10] Report on "$\gamma\gamma$ Physics", conveners P. Aurenche and G.A. Schuler, General Meeting LEP2 Physics Workshop, Geneva, Switzerland, June 1995, hep-ph/9601317.

[11] D.J. Lauber, E. McKigney, D. Miller, S. Soeldner-Rembold, private communication.

[12] A.C. Bawa, W.J. Stirling, Z. Phys. **C57** (1993) 165.

[13] B. Pötter, report DESY 97-138 (unpublished).

[14] S.J. Brodsky, T. DeGrand, J. Gunion, J. Weis, Phys. Rev **D19** (1979) 1418;
M. Drees, R.M. Godbole, Nucl. Phys. **B399** (1990) 355.

[15] G. Kramer, Springer Tracts in Mod. Phys., Vol. 102, Springer, Berlin (1984).

[16] T. Brodkorb, J.G. Körner, E. Mirkes, G.A. Schuler, Z. Phys. **C44** (1989) 415; T. Brodkorb, J.G. Körner, Z. Phys. **C54** (1992) 519.

[17] D. Graudenz, Phys. Rev. **D49** (1994) 3291.

[18] M. Klasen, G. Kramer, Z. Phys **C72** (1996) 107.

[19] C.F. v. Weizsäcker, Z. Phys. **88** (1934) 612; E.J. Williams, Kgl. Danske Vidensk. Selskab. Mat-Fiz. Medd. **13** (1935) N4.

[20] V.M. Budnev, I.F. Ginzburg, G.V. Meledin, V.G. Serbo, Phys. Rep. **15C** (1974) 181.

[21] R.K. Ellis, D. Ross, A.E. Terrano, Nucl. Phys. **178** (1981) 421.

[22] K. Fabricius, G. Kramer, G. Schierholz, I. Schmitt, Z. Phys. **C11** (1982) 315.

[23] R.K. Ellis, M.A. Furman, H.E. Haber, I. Hinchcliffe, Nucl. Phys. **B173** (1980) 397.

[24] G.P. Lepage, J. Comp. Phys. **27** (1978) 192.

[25] J.E. Huth et al., Proc. of the 1990 DPF Summer Study on High Energy Physics, Snowmass, Colorado, edited by E.L. Berger, World Scientific, Singapore, 1992, p. 134.

[26] M. Glück, E. Reya, A. Vogt, Phys. Rev. **D45** (1992) 3986;
Phys. Rev. **D46** (1992) 1973.

[27] G. Kramer, B. Pötter, DESY98-046, hep-ph/9804352.

[28] M. Klasen, G. Kramer, B. Pötter, Eur. Phys. J. **C1** (1998) 261.

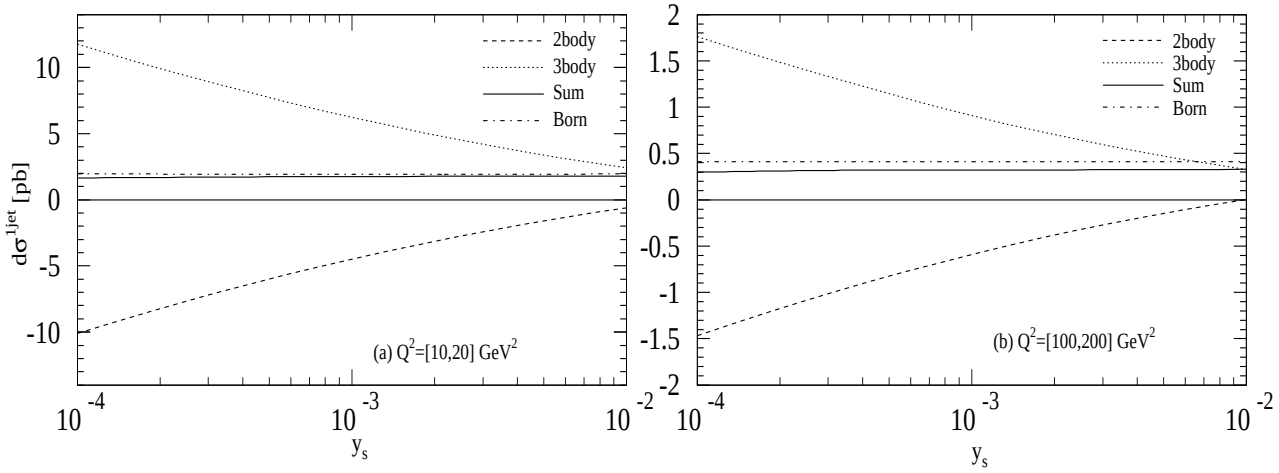

Figure 3: Single-jet inclusive direct cross section $d\sigma^{1jet}$ integrated over $E_T > 3$ GeV and $|\eta| < 2$ as a function of y_s. (a) $Q^2 \in [10, 20]$ GeV^2; (b) $Q^2 \in [100, 200]$ GeV^2.

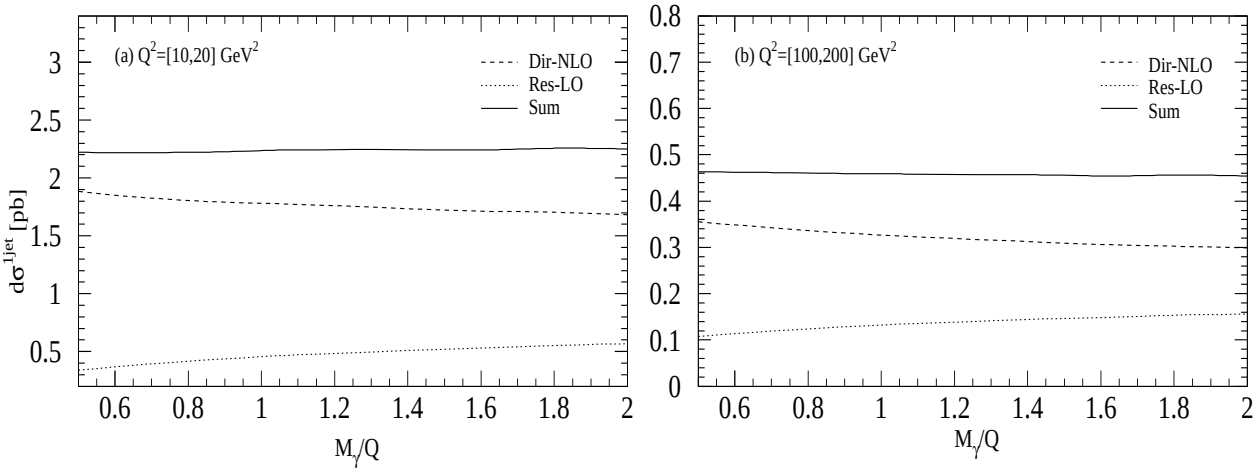

Figure 4 a,b: Single-jet inclusive direct cross section $d\sigma^{1jet}$ integrated over $E_T > 3$ GeV and $|\eta| < 2$ as a function of the normalized factorization scale M_γ/Q for the same Q^2 intervalls as in Fig. 3.

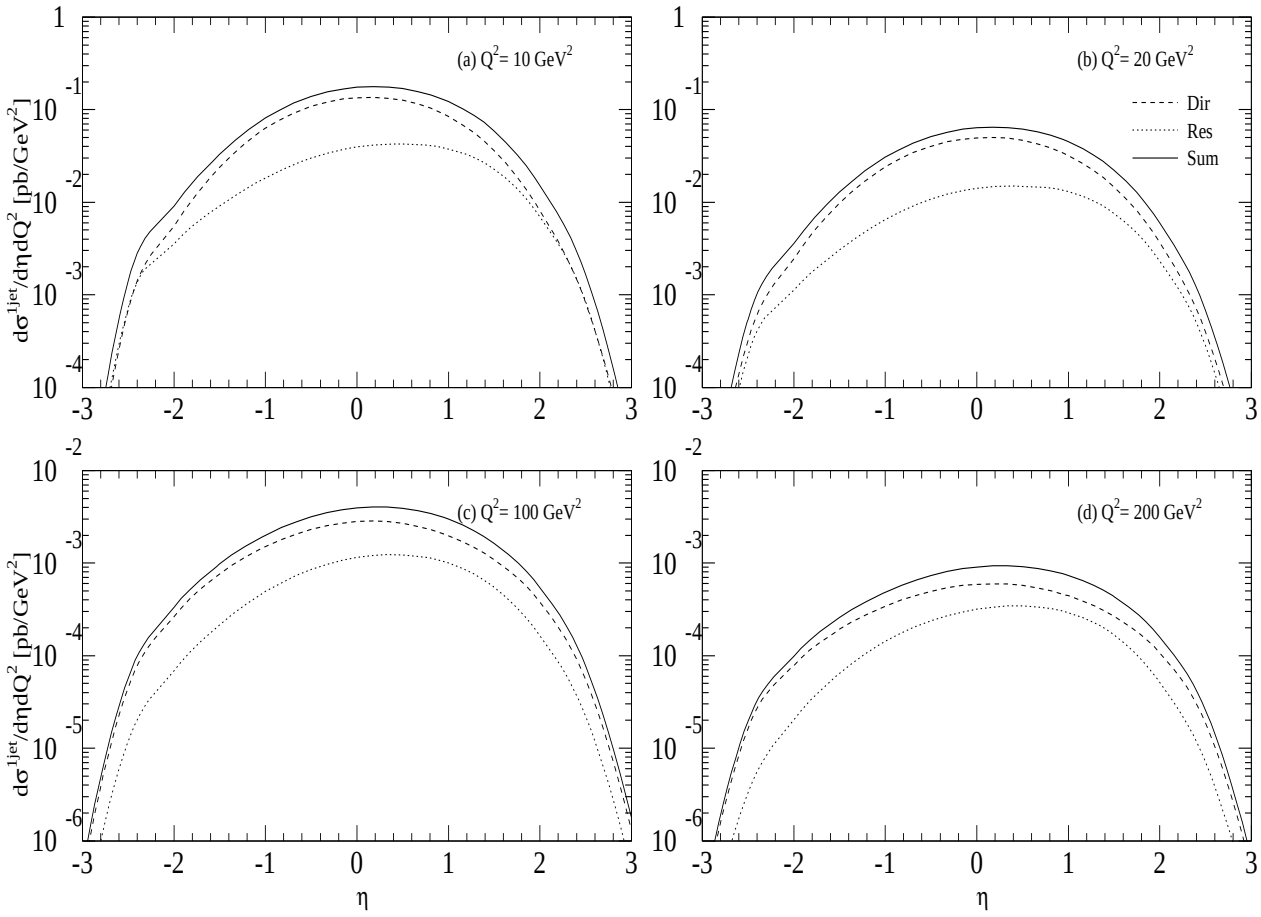

Figure 5: Inclusive single-jet cross section $d\sigma^{1jet}/d\eta dQ^2$ integrated over $E_T > 3$ GeV as a function of the rapidity η. (a) $Q^2 = 10$ GeV^2; (b) $Q^2 = 10$ GeV^2; (c) $Q^2 = 100$ GeV^2; (d) $Q^2 = 200$ GeV^2. Direct: dashed line; resolved: dotted line; sum: full line.

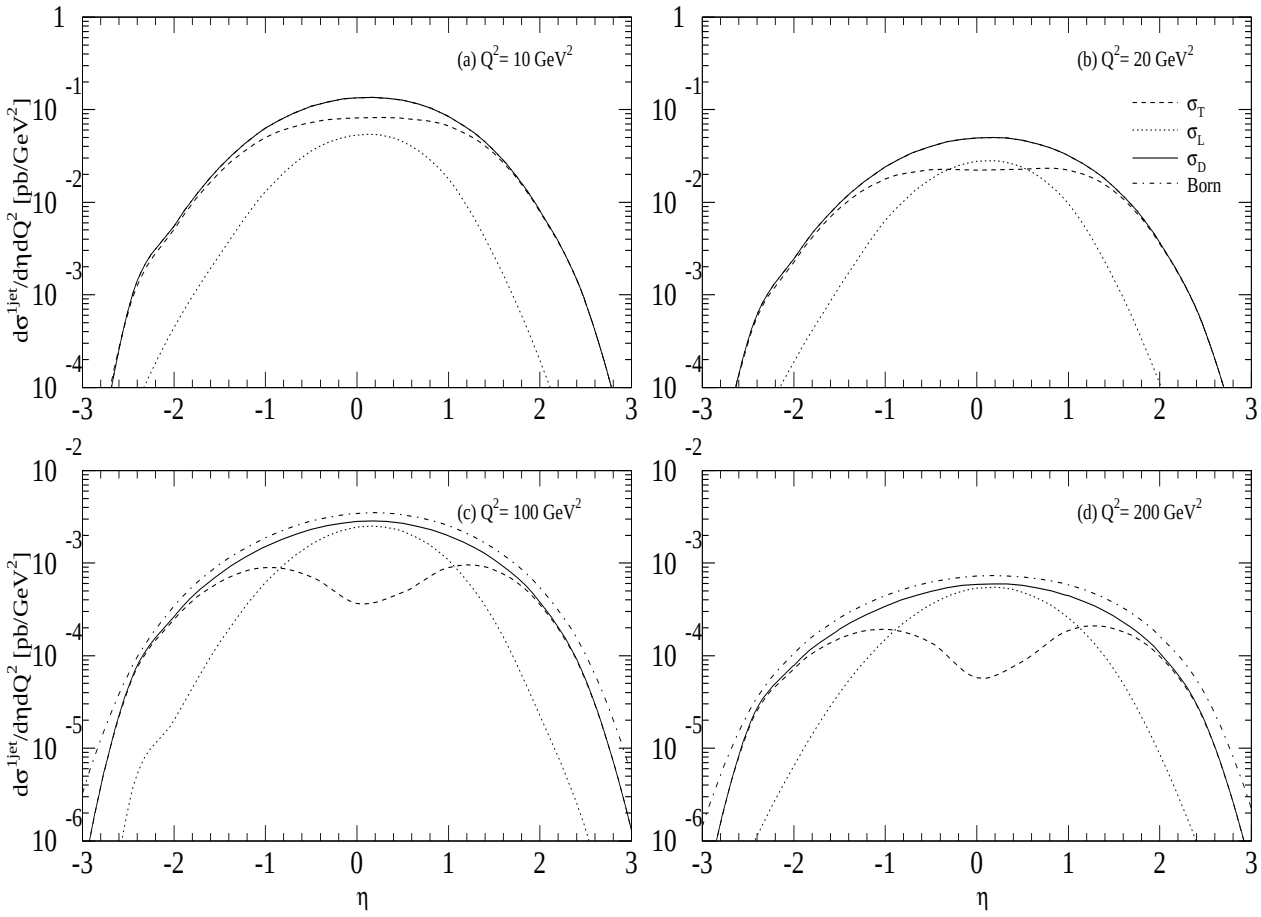

Figure 6: Direct inclusive single-jet cross section $d\sigma^{1jet}/d\eta dQ^2$ integrated over $E_T > 3$ GeV as a function of the rapidity η for the same Q^2-values as in Fig. 5 (a)–(d).

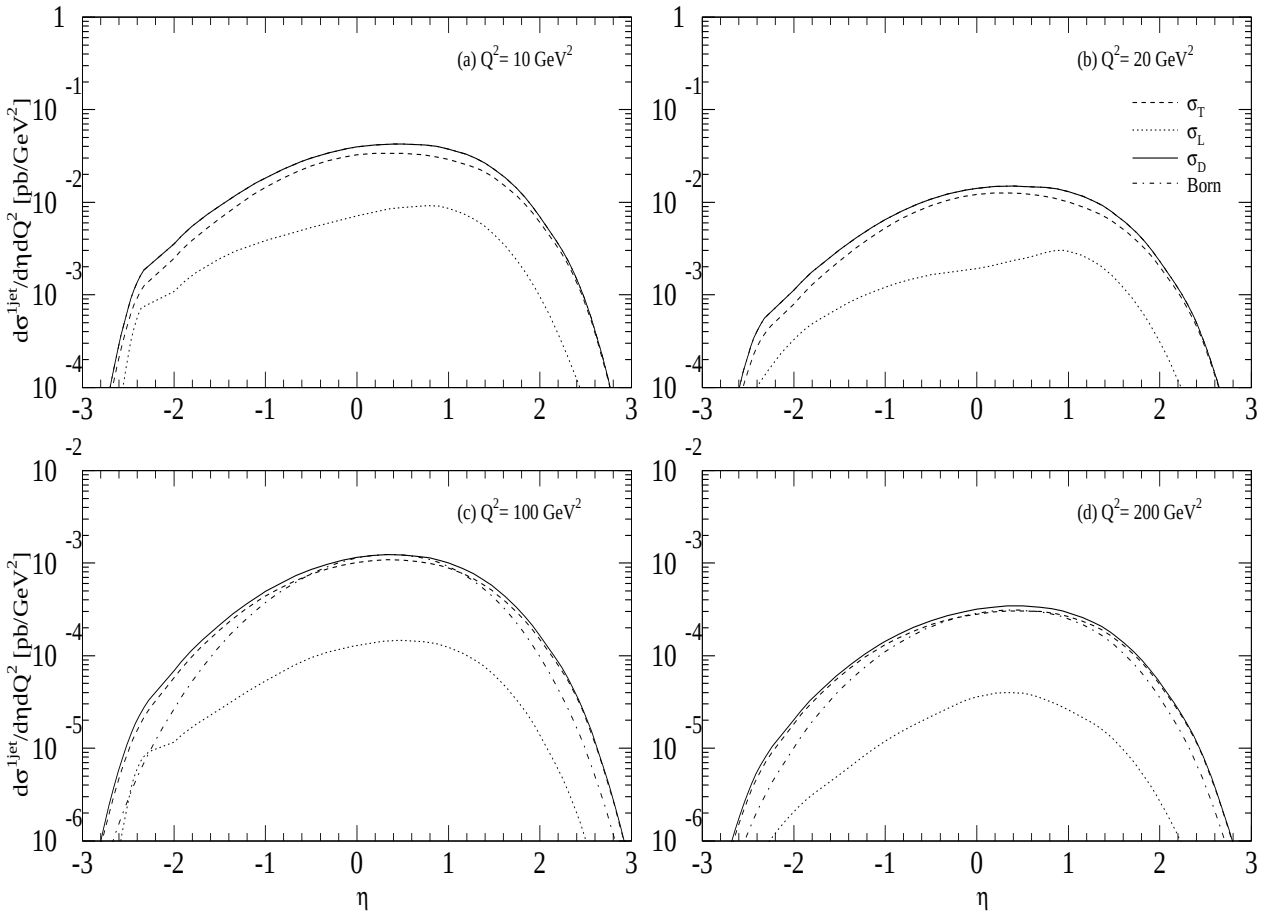

Figure 7: Resolved inclusive single-jet cross section $d\sigma^{1jet}/d\eta dQ^2$ integrated over $E_T > 3$ GeV as a function of the rapidity η for the same Q^2-values as in Fig. 5 (a)–(d).

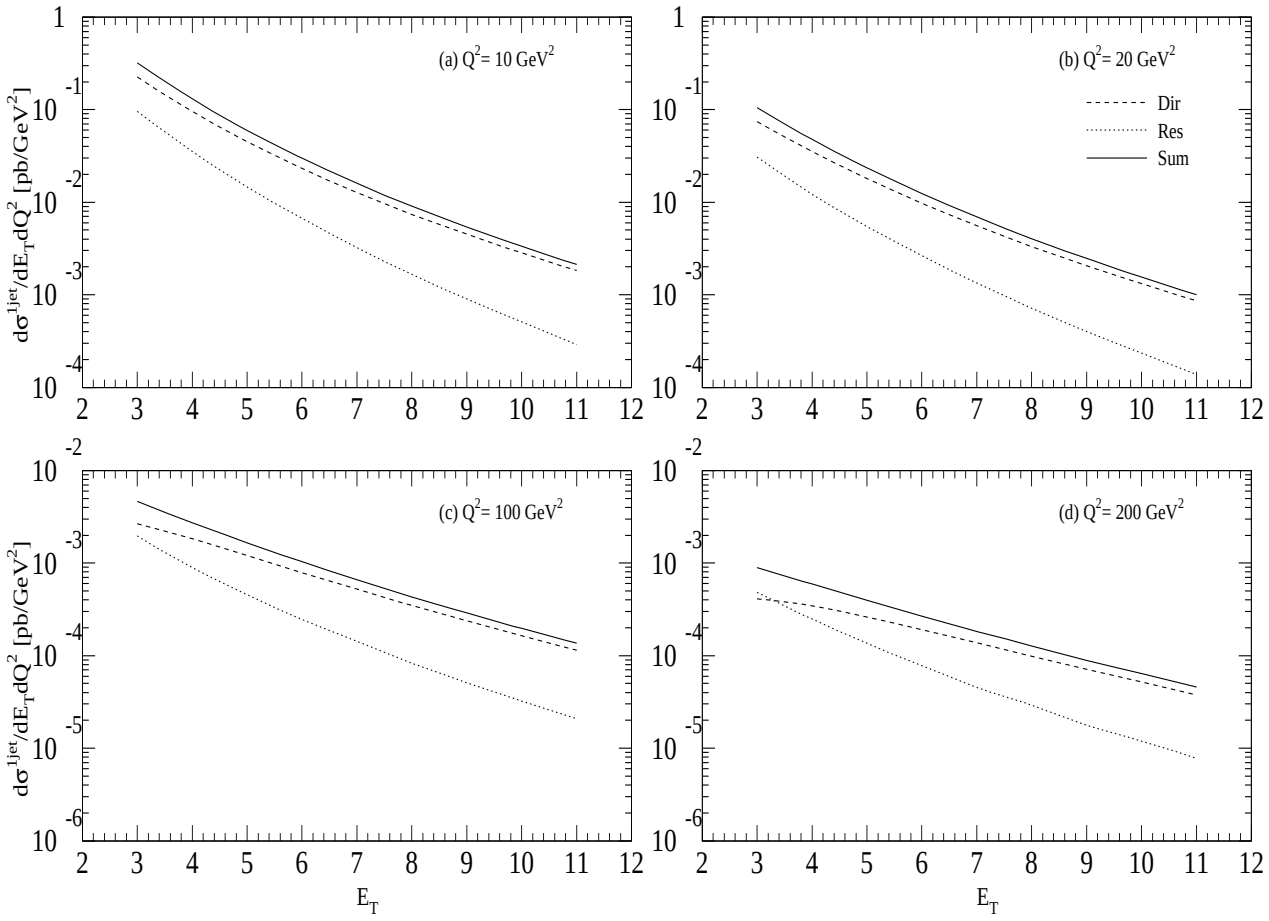

Figure 8: Inclusive single-jet cross section $d\sigma^{1jet}/dE_T dQ^2$ integrated over η as a function of the transverse momentum E_T for the same Q^2-values as in Fig. 5 (a)–(d).

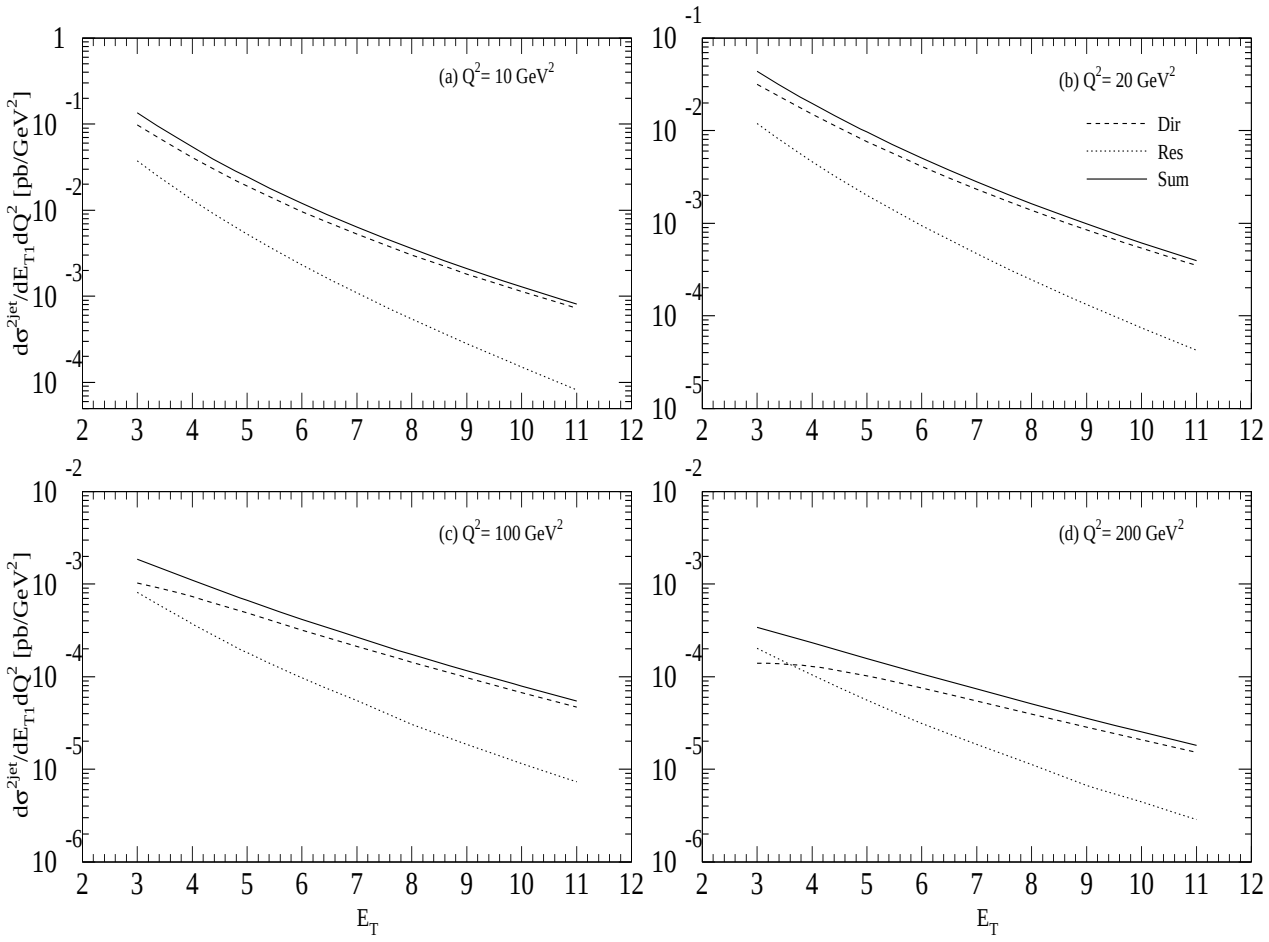

Figure 9: Inclusive dijet cross section $d\sigma^{2jet}/dE_{T_1}dQ^2$ integrated over $\eta_1, \eta_2 \in [-2, 2]$ as a function of the transverse momentum of the trigger jet E_{T_1} for the same Q^2-values as in Fig. 5 (a)–(d) for LEP1.

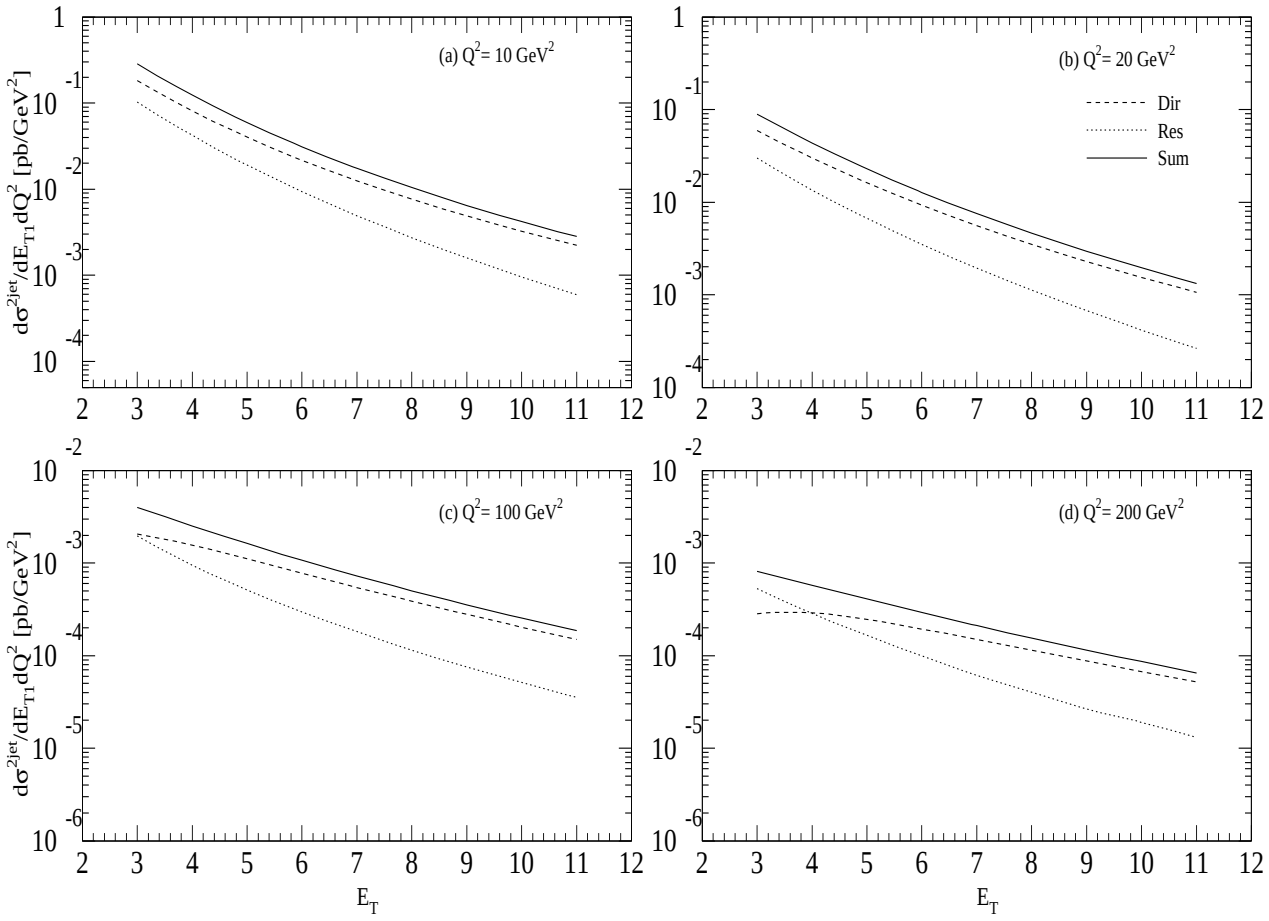

Figure 10: Inclusive dijet cross section $d\sigma^{2jet}/dE_{T_1}dQ^2$ integrated over $\eta_1, \eta_2 \in [-2, 2]$ as a function of the transverse momentum of the trigger jet E_{T_1} for the same Q^2-values as in Fig. 5 (a)–(d) for LEP2.

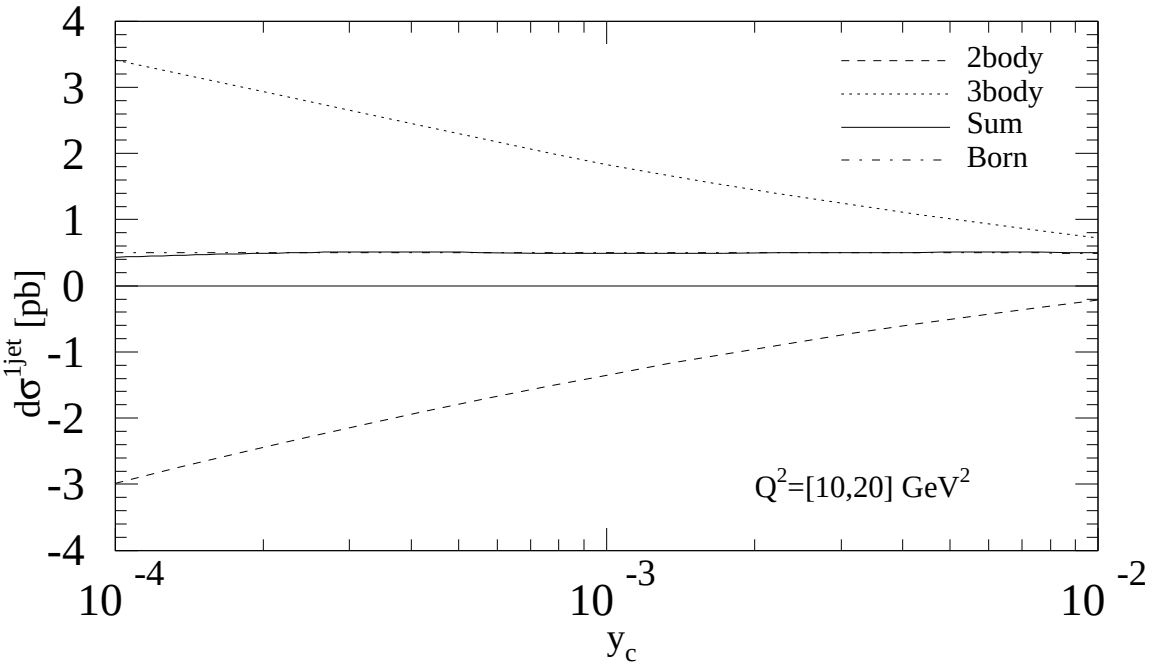
4
3
2
1
0
-1
-2
-3
-4
$d\sigma^{1jet}$ [pb]
10^{-4}
10^{-3}
10^{-2}
y_c
2body
3body
Sum
Born
Q^2=[10,20] GeV^2

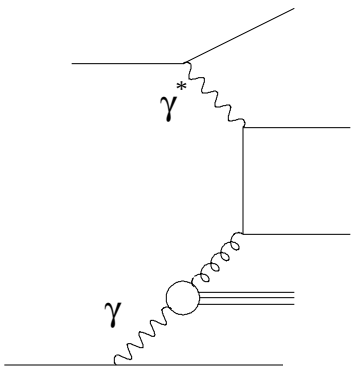
γ*
γ

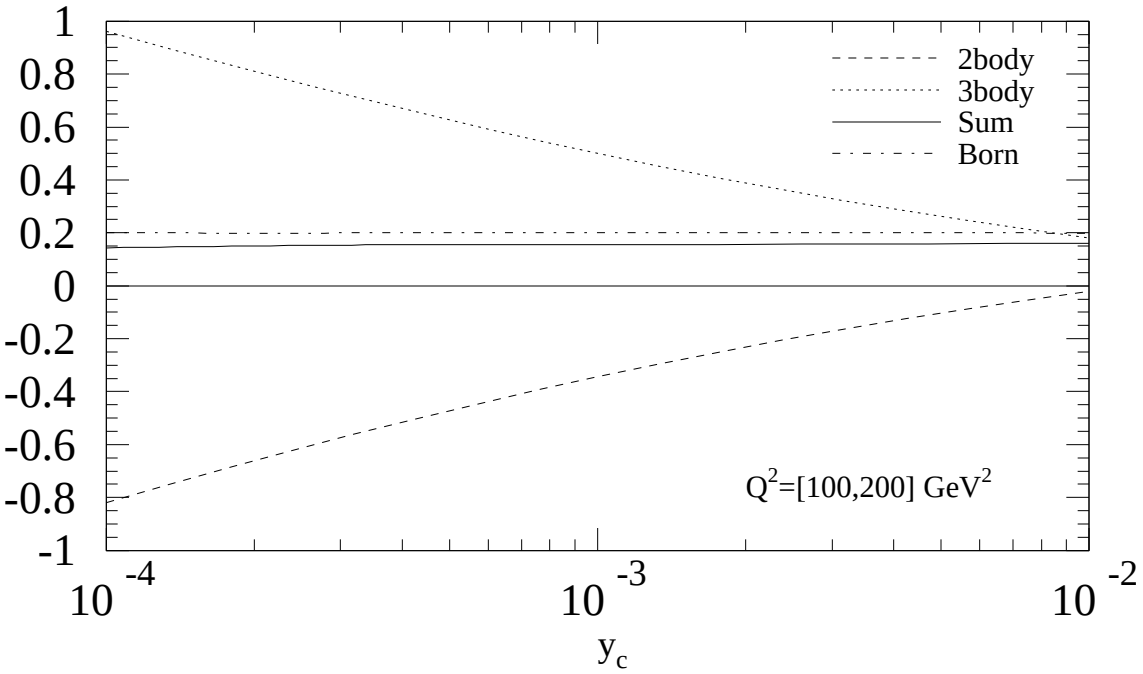
1
0.8
0.6
0.4
0.2
0
-0.2
-0.4
-0.6
-0.8
-1
10 -4
10 -3
10 -2
y_c
2body
3body
Sum
Born
Q^2=[100,200] GeV^2

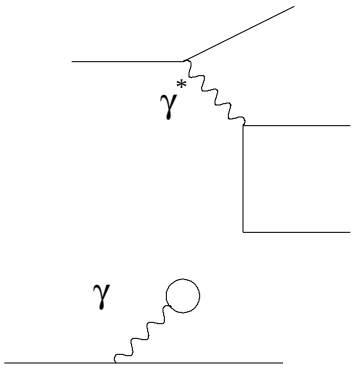

resolved